

Charge Transport and Mode Transition in Dual-Energy Electron Beam Diodes

Chubin Lin,¹ Jiandong Chen,¹ Huihui Wang,² and Yangyang Fu^{1,3,4,*}

¹*Department of Electrical Engineering, Tsinghua University, Beijing 100084, China*

²*Department of Chemical Engineering, Tsinghua University, Beijing 100084, China*

³*State Key Laboratory of Power System Operation and Control,*

Department of Electrical Engineering, Tsinghua University, Beijing 100084, China

⁴*Sichuan Energy Internet Research Institute, Tsinghua University, Sichuan 610213, China*

(Dated: February 10, 2026)

This Letter uncovers five distinct charge transport modes and their transitions in dual-energy electron beam diodes. We via first-principle particle-in-cell (PIC) simulations establish that the specific mode (e.g., space charge oscillations) and the current transport characteristics are essentially governed by the interplay between the electron beam energy and injected current density. A generalized analysis is conducted for n -component electron beams, and a theoretical piecewise function is for the transmitted current density proposed, which agrees well with the PIC results under designed conditions. The discovery provides a mechanistic picture of multiple electron beam transport in diodes, paving the way for novel designs of high-performance modern vacuum electronic devices.

Introduction—Electron beams [1–3], as directed electron streams characterized by their current density [4–6], energy spectrum [7–9] and spatiotemporal evolutions [10, 11], are indispensable drivers for various applications [12–15], such as Pierce diodes [16], virtual cathode oscillators [17, 18], thermionic energy converters [19–21], compact terahertz sources [22–26], and ultrafast switches [27]. In electron beam driven diodes, an injected intense electron current, accompanied by significant space charge effects [28, 29], can limit the transmitted current to a maximum, which is known as the space-charge-limited (SCL) current J_{SCL} [30, 31]. The charge transport in diodes with mono-energetic electron beams has been well understood, and the maximum transmitted current obeys the prediction by the SCL current J_{SCL} [32–34]. Previously, first-principle particle-in-cell (PIC) simulations showed that in mono-energetic electron beam driven diodes, the transmitted current J_{tran} is as a function of the injected current J_{inj} , i.e., $J_{\text{tran}} = J_{\text{inj}}$ for $J_{\text{inj}} \leq J_{\text{SCL}}$, whereas J_{tran} becomes saturated (or oscillating with nonzero emission velocity) for $J_{\text{inj}} > J_{\text{SCL}}$ [35, 36]. If $J_{\text{inj}} > J_{\text{SCL}}$, a virtual cathode (adjacent to the cathode) can form with an oscillating potential barrier, which periodically reflects less energetic electrons released from the cathode, thereby inducing space-charge oscillations [37–39]. In the oscillation regime, existing analytical solutions can predict the spatial profiles of diode physical quantities (e.g., electric potential) [35]. The scaling law for the space charge oscillation frequency has been theoretically derived and validated via PIC simulations [40]. However, the SCL current fails when electrons have distributed energies (e.g., the Maxwell distribution for electron thermal motion) or when multi-energy electron beams form, since space-charge oscillations can be altered, leading to different steady states [35]. Although well-studied in mono-energy beams, the SCL current and oscillatory dynamics in diodes with discrete energy components present emergent complexities, and a complete theoretical framework remains elusive.

In this Letter, we report five complete charge transport modes and their transitions in diodes driven by precisely controlled dual-energy electron beams. For the first time, we, via PIC simulations, demonstrate the control of five distinct operation modes by independently modulating high- and low-energy electron beams, and identify that the velocity ratio dictates mode transitions, whereas the injected current ratio determines transmitted current scaling characteristics. The results provide key insights into multi-electron beam-driven diodes, which are essential for promoting modern technologies in vacuum electronics.

Physical model—The schematic of the planar vacuum diode with cathode-anode gap distance of d_{gap} driven by dual-energy electron beams is shown in Fig. 1. Two groups of electrons are injected from the cathode, including low-energy electrons e_1 at an initial velocity $v_1 = \beta_1 \sqrt{2eV/m_e}$ with an injected current density J_1 and high-energy electrons e_2 at an initial velocity $v_2 = \beta_2 \sqrt{2eV/m_e}$ with an injected current density J_2 , where β_1 and β_2 are dimensionless initial velocity factors, e is the elementary charge, V is the gap voltage, and m_e is the electron mass. The different groups of electron beams, generated from field emission [41, 42], thermal-field emission [43], photo-emission [44], or laser-driven accelerators [7], can be independently transported. The total injected current density J_0 is the sum of injected current density of e_1 and e_2 , i.e., $J_0 = J_1 + J_2$. Here, the initial velocity and injected current of each electron beam can be independently controlled, which are characterized by two dimensionless parameters, i.e., the velocity ratio $v_1/v_2 = \beta_1/\beta_2 \in (0, 1)$ and the injected current ratio J_1/J_2 (can be controlled greater or less than one).

The virtual cathode with the minimum potential ϕ_{vc} at the position x_{vc} is generated self-consistently by both electron beams, which can block electrons when their initial energy $\mathcal{E}_0 < -e\phi_{\text{vc}}$. Here we have $\mathcal{E}_0 = \mathcal{E}_{e1}$ for e_1 , $\mathcal{E}_0 = \mathcal{E}_{e2}$ for e_2 , and $\mathcal{E}_{e1} < \mathcal{E}_{e2}$, thus, electrons with different energies exhibit distinct dynamical behaviors responding to the electric potential. As shown in Fig. 1, low-energy electrons e_1 without sufficient kinetic energy can be predominantly reflected by the virtual cathode potential barrier, whereas high-energy electrons e_2 can overcome potential barriers, and can be mostly

* fuyangyang@tsinghua.edu.cn

transported and absorbed by the anode. The electron reflection point is determined by the critical condition where the reflection potential $\phi_{\text{ref}} = -\mathcal{E}_0/e$, and here we have $\phi_{\text{ref},1} = -\mathcal{E}_{e1}/e$ for e_1 and $\phi_{\text{ref},2} = -\mathcal{E}_{e2}/e$ for e_2 . Thus, the electron reflection point position for low-energy electrons is closer to the cathode than for high-energy electrons, i.e., $x_{\text{ref},1} < x_{\text{ref},2}$.

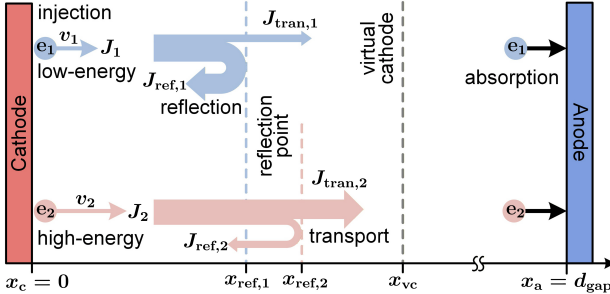


FIG. 1. Schematic of the dual-energy electron beam driven diode, in which the cathode injection current consists of low-energy and high-energy electrons. Low-energy electrons tend to be reflected mostly, whereas high-energy electrons can be transmitted predominantly to the anode. $x_c = 0$ is the cathode, and $x_a = d_{\text{gap}}$ is the anode. Note that the cathode-to-virtual cathode region is enlarged and $x_{\text{ref},1} < x_{\text{ref},2} < x_{\text{vc}} \ll d_{\text{gap}}$, where $x_{\text{ref},1}$ and $x_{\text{ref},2}$ are the reflection points, and x_{vc} is the virtual cathode position.

Operation modes—Each electron beam (low-energy e_1 and high-energy e_2) exhibits three possible charge transport states: fully transported mode (T-mode), oscillation mode (O-mode) with intermittent transport and reflection, and fully reflected mode (R-mode). While state permutations permit $3^2 = 9$ theoretical transport modes, stronger space-charge suppression on e_1 than e_2 constrains the system to five dynamical modes (M1–M5). Notably, both e_1 and e_2 cannot be fully reflected simultaneously; otherwise, the virtual cathode is unable to sustain [35]. By systematically tuning the control parameters of each electron beam, e.g., initial velocity and injected current density, we identify five observationally distinct operation modes in dual-energy electron beam driven diodes, as shown in Table I. The "NA" indicates the combination does not exist.

TABLE I. Operation modes in the dual-energy electron beam driven diodes.

$e_1 \backslash e_2$	T	O	R
T	M1 ($T_1 - T_2$)	M2 ($O_1 - T_2$)	M3 ($R_1 - T_2$)
O	NA	M5 ($O_1 - O_2$)	M4 ($R_1 - O_2$)
R	NA	NA	NA

Figure 2 demonstrates five operation modes (M1–M5), including the electric potential distribution $\phi - x$, temporal evolution of the cathode surface electric field $E_s - t$, and phase space of spatially averaged electron density versus cathode surface electric field $\bar{n}_e - E_s$ for each mode. In mode M1, the minimum gap potential follows $\phi_{\text{min}} > \phi_{\text{ref},1} > \phi_{\text{ref},2}$ [see Fig. 2(a1)], which enables fully transport of both low-energy

electrons e_1 and high-energy electrons e_2 in steady state. Mode M2 emerges when the intense space-charge effect occurs and lowers the electric potential, forming a virtual cathode potential ϕ_{vc} that oscillates near the reflection potential of low-energy electrons $\phi_{\text{ref},1}$. This condition, though maintain full transport for e_2 , can trigger intermittent reflection-transport cycles for e_1 , which can induce oscillations of physical quantities, such as the cathode surface electric field E_s [Fig. 2(b2)]. Since the oscillation is induced by e_1 , the oscillation frequency for M2 can be predicted by $f_{\text{os}} \propto \sqrt{J_1/\beta_1}$ [40]. Mode M3 is established when the virtual cathode potential stabilizes below $\phi_{\text{ref},1}$ but above $\phi_{\text{ref},2}$, i.e., $\phi_{\text{ref},1} > \phi_{\text{min}} > \phi_{\text{ref},2}$, [Fig. 2(a3)], resulting in a new steady state where e_1 is completely reflected but e_2 is fully transported. In Fig. 2(a4), by further increasing the injected current, M4 occurs when the virtual cathode potential is sufficiently low to oscillate near the reflection potential of high-energy electrons $\phi_{\text{ref},2}$. Thus, e_1 can be completely reflected and reabsorbed by the cathode whereas e_2 has intermittent transport and reflection, inducing periodic oscillation with the oscillation frequency scaling as $f_{\text{os}} \propto \sqrt{J_2/\beta_2}$. Especially, when the energies of e_1 and e_2 are rather close (e.g., $v_1/v_2 = \sqrt{\mathcal{E}_{e1}/\mathcal{E}_{e2}} = 0.95$), M5 is formed and the virtual cathode potential oscillates between $\phi_{\text{ref},1}$ and $\phi_{\text{ref},2}$ [Fig. 2(a5)]. Then both the low- and high-energy electrons can oscillate at their respective frequencies, generating a combined oscillation waveform [see Fig. 2(b5)]. The phase space distributions of $\bar{n}_e - E_s$ for five operation modes (M1–M5) are shown in Figs. 2(c1)–(c5), respectively, which confirm that loop trajectories are formed in the oscillation modes.

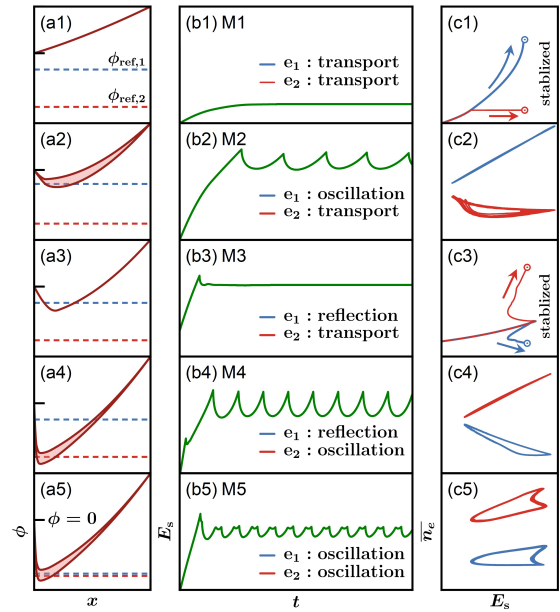


FIG. 2. Five operation modes in the dual-energy electron beam driven diode. The panels from left to right correspond to (a1)–(a5) $\phi - x$, (b1)–(b5) $E_s - t$, and (c1)–(c5) $\bar{n}_e - E_s$. The combinations of the emitted electrons (e_1 and e_2) result in five operation modes, i.e., M1 (both e_1 and e_2 transmitted), M2 (e_1 oscillated and e_2 transmitted), M3 (e_1 reflected and e_2 transmitted), M4 (e_1 reflected and e_2 oscillated), and M5 (both e_1 and e_2 oscillated).

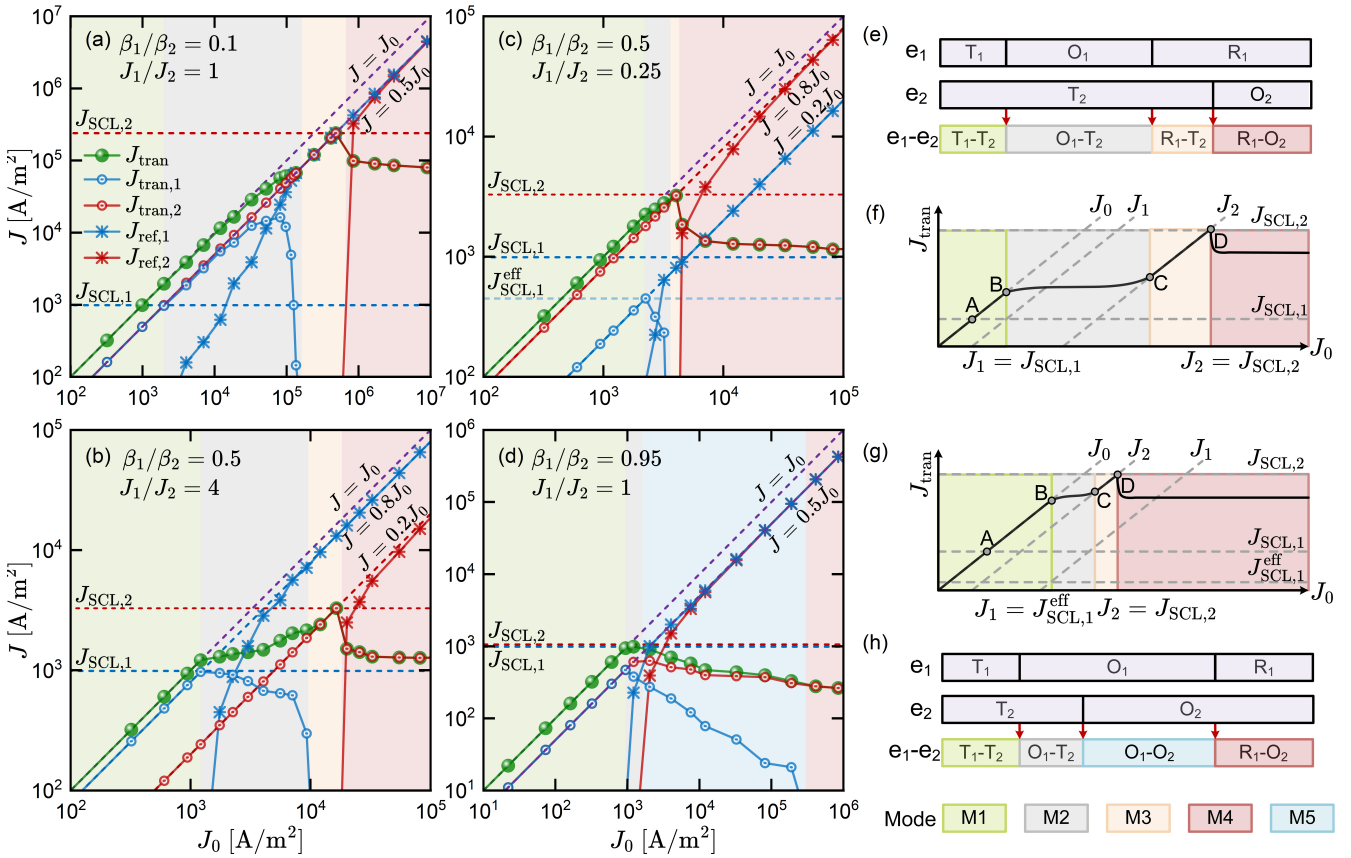


FIG. 3. Total transmitted current J_{tran} ($J_{\text{tran}} = J_{\text{tran},1} + J_{\text{tran},2}$ with $J_{\text{tran},1}$ for low-energy electron e_1 and $J_{\text{tran},2}$ for high-energy electron e_2) and reflected current J_{ref} ($J_{\text{ref}} = J_{\text{ref},1} + J_{\text{ref},2}$ with $J_{\text{ref},1}$ for e_1 and $J_{\text{ref},2}$ for e_2) as a function of the injected current J_0 ($J_0 = J_1 + J_2$ with J_1 for e_1 and J_2 for e_2) under different conditions. Governing parameters ($\beta_1/\beta_2, J_1/J_2$) = (0.1, 1) for (a), (0.5, 4) for (b), (0.5, 0.25) for (c), and (0.95, 1) for (d). (e) Schematic of the operation mode transition for panel (a). (f)–(g) Illustrations of the transmitted current for panels (b) and (c). (h) Schematic of the operation mode transition for panel (d).

Transmitted current characteristics—The transmitted current characteristics for mono-energetic electrons have been explicitly demonstrated in previous studies [35, 40]. The SCL current, as the critical current threshold [35], is expressed as

$$J_{\text{SCL}} = \frac{4\epsilon_0}{9} \sqrt{\frac{2e}{m_e}} \frac{V^{3/2}}{d^2} \left(\beta + \sqrt{1 + \beta^2} \right)^3, \quad (1)$$

where β quantifies the initial velocity of emitted electrons. The transmitted current J_{tran} equals the injected current J_{inj} for $J_{\text{inj}} \leq J_{\text{SCL}}$ while becomes saturatee for $J_{\text{inj}} > J_{\text{SCL}}$. However, in dual-energy electron beam driven diodes, each electron beam possesses its own SCL current ($J_{\text{SCL},1}$ for e_1 and $J_{\text{SCL},2}$ for e_2) since β is equal to β_1 or β_2 , respectively, which leads to significantly complex transmitted current behaviors.

By separately tuning the control parameters for dual-energy electron beams, the transmitted current scaling and charge transport mode transition are determined, as shown in Fig. 3. The ratio of initial velocity for two electron beams, β_1/β_2 , plays a significant role in determining the charge transport mode transition. For electron beams with a large difference in velocity (energy) (e.g., $\beta_1/\beta_2 = 0.1$), the transmitted current characteristics are illustrated in Fig. 3(a). When the injected

current J_0 is sufficiently low (below the SCL current of the low-energy electrons $J_{\text{SCL},1}$), both low- and high-energy electrons can be fully transmitted [mode M1]. When the injected current for low-energy electrons J_1 exceeds their corresponding SCL current $J_{\text{SCL},1}$, the transport of low-energy electrons e_1 is suppressed while the high-energy electrons e_2 can still be transported completely [mode M2]. Notably, in this regime, the transmitted current for low-energy electrons $J_{\text{tran},1}$ falls below J_1 and the reflected current for low-energy electrons $J_{\text{ref},1}$ increases substantially, maintaining the current conservation $J_1 = J_{\text{tran},1} + J_{\text{ref},1}$. As the injected current further increases, low-energy electrons can be fully reflected with $J_{\text{ref},1} = J_{\text{inj},1}$, while high-energy electrons remain fully transported [mode M3]. Once the injected current for high-energy electrons J_2 is larger than their corresponding SCL current $J_{\text{SCL},2}$, high-energy electrons e_2 are partially reflected, accompanied with the entire reflection of e_1 [mode M4]. Consequently, while increasing the total injected current J_0 , the charge transport modes undergo a well-defined pathway: M1 → M2 → M3 → M4, which can be abstracted to discrete eigen-states defined by combinatorial permutations of the transport modes for both energy components [see Fig. 3(e)].

Figure 3(b) maps the transmitted current characteristics under parameter conditions of $\beta_1/\beta_2 = 0.5$ and $J_1/J_2 = 4$, demonstrating more universal behaviors of the transmitted currents. Note that the critical mode transitions are quantitatively defined by the intersection points where the injected current of each electron beam component reaches its corresponding SCL current. As illustrated in the schematic diagram [see Fig. 3(f)], we identify several critical points (A-D) to visually mark the evolution of transmitted current. At point A, the total injected current $J_0 = J_{SCL,1}$ and all the electrons can be transported steadily, i.e., M1 with the total transmitted current $J_{tran} = J_0$. The transition from M1 to M2 occurs abruptly when the injected current of low-energy electrons reaches their SCL current [point B], i.e., $J_1 = J_{SCL,1}$, and then J_{tran} deviates from J_0 . Theoretically, the transition point is expected when $J_1 < J_{SCL,1}$; however, due to the significant energy difference between the two electron beams and the relatively minor space charge effect of the high-energy electrons, one can consider the critical transition at point B. The point C marks the M2–M3 transition where $J_{tran} = J_2$ and $J_{tran,1} = 0$, indicating that only the single electron beam (e_2) is transmitted in the diode. At point D, $J_2 = J_{SCL,2}$ and the transmitted current achieves its maximum, simultaneously signifying the M3–M4 transition.

In addition, the injected current ratio J_1/J_2 serves as a key control parameter, modulating the mode transition pathway. Figure 3(c) shows the transmitted current characteristics under low-energy electron-dominated injection conditions ($J_1/J_2 = 4 > 1$), which shows an obvious difference from that in high-energy electron-dominated injection conditions ($J_1/J_2 = 0.25 < 1$) [see Fig. 3(b)]. Notably, low-energy electrons e_1 undergo abnormal reflection before reaching their conventional SCL current $J_{SCL,1}$, leading to an effective SCL current $J_{SCL,1}^{\text{eff}}$ smaller than $J_{SCL,1}$. This is because the virtual cathode induced by space charge effects, dominated by high-energy electron injection, easily suppresses the transport of low-energy electrons. As illustrated in Fig. 3(g), the critical point B for M1–M2 transition is defined as the intersection point with $J_1 = J_{SCL,1}^{\text{eff}}$, which occurs before reaching the conventional threshold $J_1 = J_{SCL,1}$.

The charge transport mode transition when the two electron beams have nearly identical energies (e.g., $\beta_1/\beta_2 = 0.95$) is shown in Fig. 3(d). Due to the negligible difference between the SCL currents of the two electron beams (e_1 and e_2), the system exhibits behavior analogous to that of a single electron beam in terms of current transmission. That is, two groups of electrons can be treated as the same electrons while determining the transmitted current. When the total injected current J_0 reaches the SCL current, the transport for the two groups of electrons can be simultaneously suppressed with partial reflection [M5, also see Fig. 2(a5)]. However, the low-energy electrons can be fully reflected when the total current is sufficiently large [see Fig. 3(d)]. Figure 3(h) presents the charge transport mode transition pathway (M1 → M2 → M5 → M4) for $\beta_1/\beta_2 \rightarrow 1$, which differs from the observed pathway for $\beta_1/\beta_2 < 1$ [see Fig. 2(e)].

A more generalized analysis can be conducted for n -component electron beams, namely $\{e_1, e_2, \dots, e_n\}$ with ener-

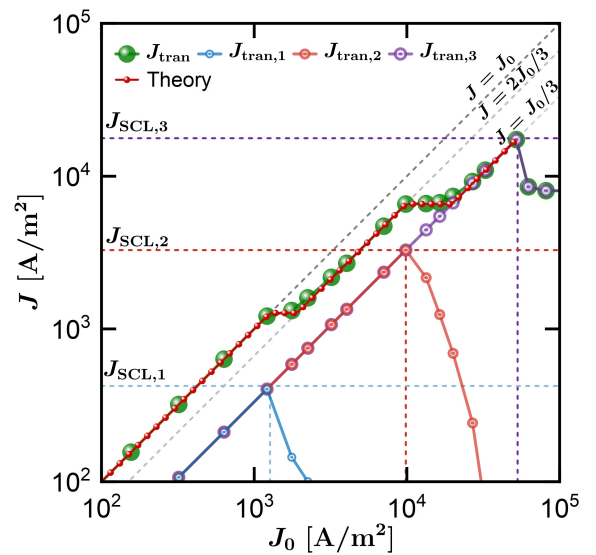


FIG. 4. Transmitted current density J_{tran} versus the total injected current density J_0 . The prediction from the proposed theoretical formula [Eq. (3)] agrees well with PIC simulation results, for example, with the electron beam number $n = 3$.

gies at $\mathcal{E}_{e1} < \mathcal{E}_{e2} < \dots < \mathcal{E}_{en}$. Each electron beam e_i ($1 \leq i \leq n$) exhibits three possible transport states $S_i \in \{2, 1, 0\}$, in which $S_i = 2$ for T-mode, $S_i = 1$ for O-mode, and $S_i = 0$ for R-mode, respectively. The operation modes in diodes with n -component electron beams can be labeled as $(S_1 S_2 \dots S_n)$, yielding 3^n possible combinations. However, the space-charge effect preferentially suppresses the transport of lower-energy electrons, resulting in $S_n \geq \dots \geq S_2 \geq S_1$, and thus the number of operation modes is determined as C_{n+2}^2 . Since one specific operation mode with all the electron beams simultaneously reflected is physically inadmissible [$(S_1 S_2 \dots S_n) \neq (00\dots0)$], the number of potential operation modes with n -component electron beams is determined by

$$N_{\text{mode}} = C_{n+2}^2 - 1 = n(n+3)/2. \quad (2)$$

Here, five operation modes ($N_{\text{mode}} = 5$) are determined for $n = 2$. If one considers identical injected current for n -component electron beams, $J_1 = J_2 = \dots = J_n = J_0/n$, with substantial energy differences. The transmitted current J_{tran} versus the total injected current J_0 exhibits a stepwise growth [see Fig. 4], and the transmitted current for e_i reaches its maximum $J_{\text{tran},i} = J_0/n = J_{\text{SCL},i}$ when $J_i = J_{\text{SCL},i}$. If $J_i > J_{\text{SCL},i}$ for e_i , the transmitted component progressively decreases to zero, and the mode transition T → O → R occurs. Generally, with an increasing J_0 , the intensified space-charge effects lead to complete reflections of electron beams e_i in the energy sequence, showing stepwise growth in transmitted current. The total transmitted current can be described as

$$J_{\text{tran}}(J_0) = \begin{cases} \frac{n+1-i}{n} J_0, & J_0 \in [J_a, J_b], \\ (n+1-i) J_{\text{SCL},i}, & J_0 \in [J_b, J_c], \end{cases} \quad (3)$$

where $J_a = (n+2-i)nJ_{SCL,i-1}/(n+1-i)$, $J_b = nJ_{SCL,i}$, $J_c = (n+1-i)nJ_{SCL,i}/(n-i)$, and i varies from 1 to n . The maximum transmitted current $J_{\text{tran}}^{\max} = J_{SCL,n}$, independent of the injected current J_0 , is reached when the highest-energy electron beam e_n reaches its SCL current, i.e., $J_n = J_{SCL,n}$.

Conclusion—In conclusion, we explicitly determined five complete modes for charge transport in dual-energy electron beam driven diodes, which are modulated by controlling the two electron beam parameters. The initial velocity ratio and the injected current ratio are identified as governing parameters; the former determines the charge transport modes and

their transitions, while the latter modulates the characteristics of the transmitted current. The discovery provides a fundamental advance in multi-energy beam physics, enabling precise tuning strategies for electron beam-driven diodes, especially for applications in modern vacuum electronic devices.

Acknowledgments—The authors acknowledge the financial support from the Fundamental and Interdisciplinary Disciplines Breakthrough Plan of the Ministry of Education of China (Grant No. JYB2025XDXM312).

Data availability—The data that support the findings of this study are available from the authors upon reasonable request.

[1] S. E. Tsimring, *Electron Beams and Microwave Vacuum Electronics* (John Wiley & Sons, Hoboken, 2007).

[2] D. B. Go, *Ionization and Ion Transport (Second Edition)*, 2053–2563 (IOP Publishing, 2022).

[3] V. Sharma and K. Hara, *Phys. Plasmas* **32**, 113103 (2025).

[4] Y. Li, L. Xia, N. Li, S. Tang, Y. Ge, J. Wang, B. Xiao, Y. Cheng, L. K. Ang, and G. Meng, *Nat. Commun.* **16**, 5583 (2025).

[5] M. D. Campanell, A. V. Khrabrov, and I. D. Kaganovich, *Phys. Rev. Lett.* **108**, 235001 (2012).

[6] M. D. Campanell and M. V. Umansky, *Phys. Rev. Lett.* **116**, 085003 (2016).

[7] J. Wenz, A. Dopp, K. Khrennikov, S. Schindler, M. F. Gilljohann, H. Ding, J. Gotzfried, A. Buck, J. Xu, M. Heigoldt, W. Helml, L. Veisz, and S. Karsch, *Nat. Photonics* **13**, 263 (2019).

[8] M. A. Furman and M. T. F. Pivi, *Phys. Rev. ST Accel. Beams* **5**, 124404 (2002).

[9] J. Chen and Y. Fu, *Phys. Rev. E* **111**, 065214 (2025).

[10] Y. Heri and P. Zhang, *IEEE Trans. Electron Devices* **72**, 2591 (2025).

[11] L. K. Ang and P. Zhang, *Phys. Rev. Lett.* **98**, 164802 (2007).

[12] P. Zhang, A. Valfells, L. K. Ang, J. W. Luginsland, and Y. Y. Lau, *Appl. Phys. Rev.* **4**, 011304 (2017).

[13] J. H. Pagán Muñoz, X. Wang, M. Horányi, V. Kvon, L. Heijmans, M. Chaudhuri, M. van de Kerkhof, A. M. Yakunin, P. Krainov, and D. Astakhov, *Phys. Rev. Lett.* **133**, 115301 (2024).

[14] O. Dubrovski, J. Yang, F. Veloso, D. B. Go, H.-C. Chang, and P. Rumbach, *Phys. Rev. Lett.* **133**, 105301 (2024).

[15] J. Chen and Y. Fu, *Phys. Rev. Appl.* **23**, 054059 (2025).

[16] A. Ender, H. Kolinsky, V. Kuznetsov, and H. Schamel, *Phys. Rep.* **328**, 1 (2000).

[17] W. Jiang, *Plasma* **7**, 29 (2024).

[18] S. Mumtaz, H. S. Uhm, and E. H. Choi, *Phys. Rep.* **1069**, 1 (2024).

[19] A. Sitek, K. Torfason, A. Manolescu, and A. Valfells, *Phys. Rev. Appl.* **15**, 014040 (2021).

[20] K. A. Abdul Khalid, T. J. Leong, and K. Mohamed, *IEEE Trans. Electron Devices* **63**, 2231 (2016).

[21] C. Lin, J. Chen, and Y. Fu, *Appl. Phys. Lett.* **124**, 074103 (2024).

[22] J. Chen, C. Lin, P. Zhang, J. P. Verboncoeur, L. K. Ang, and Y. Fu, *Phys. Rev. Lett.*, (2026).

[23] B. S. Alexandersson, K. Torfason, A. Manolescu, and A. Valfells, *Phys. Rev. Lett.*, (2026).

[24] A. Pedersen, A. Manolescu, and A. Valfells, *Phys. Rev. Lett.* **104**, 175002 (2010).

[25] T. Zhang, R. Ischebeck, U. Niedermayer, T. Schietinger, and P. Juranić, *Phys. Rev. Accel. Beams* **28**, 054501 (2025).

[26] M. Kumar, B. Ersfeld, J. Lee, D. Park, S. Kim, I. Nam, M. Kim, S. Jeon, D. A. Jaroszynski, H. Suk, and M. S. Hur, *Phys. Rev. Lett.* **134**, 015001 (2025).

[27] M. Samizadeh Nikoo, A. Jafari, N. Perera, M. Zhu, G. Santoruvo, and E. Matioli, *Nature* **579**, 534 (2020).

[28] C. K. Birdsall and W. B. Bridges, *Electron Dynamics of Diode Regions* (Academic, New York, 1966).

[29] M. D. Campanell, C. Y. Wang, and K. L. Nguyen, *Phys. Rev. Lett.* **134**, 145301 (2025).

[30] C. D. Child, *Phys. Rev.* **32**, 492 (1911).

[31] G. Jaffé, *Phys. Rev.* **65**, 91 (1944).

[32] Y. B. Zhu, P. Zhang, A. Valfells, L. K. Ang, and Y. Y. Lau, *Phys. Rev. Lett.* **110**, 265007 (2013).

[33] X. Zhu, N. R. Sree Harsha, and A. L. Garner, *J. Appl. Phys.* **134**, 113301 (2023).

[34] A. L. Garner, N. R. S. Harsha, and A. M. Loveless, *J. Appl. Phys.* **137**, 234501 (2025).

[35] T. Lafleur, *Plasma Sources Sci. Technol.* **29**, 065002 (2020).

[36] T. Lafleur, *Plasma Sources Sci. Technol.* **31**, 114008 (2022).

[37] W. B. Bridges and C. K. Birdsall, *J. Appl. Phys.* **34**, 2946 (1963).

[38] C. Lin and Y. Fu, *IEEE Electron Device Lett.* **46**, 1857 (2025).

[39] Y. B. Zhu and D. H. Kong, *IEEE Trans. Electron Devices* **70**, 5959 (2023).

[40] C. Lin, J. Chen, H. Wang, P. Zhang, L. K. Ang, J. P. Verboncoeur, and Y. Fu, *Phys. Rev. E* **112**, L063201 (2025).

[41] R. G. Forbes, *R. Soc. Open Sci.* **6**, 190912 (2019).

[42] J. Ying, L. Liu, L. Zheng, D. Su, X. He, J. Ma, H. Xuan, and D. Zhang, *Phys. Rev. X* **15**, 021095 (2025).

[43] K. L. Jensen, *J. Appl. Phys.* **126**, 065302 (2019).

[44] J. Heimerl, A. Mikhaylov, H. Meier, Stefan amd Hollerer, I. Kaminer, M. Chekhova, and P. Hommelhoff, *Nat. Phys.* **20**, 945 (2024).